

Glimpse of the highly obscured HMXB IGR J16318–4848 with Hitomi*

Hitomi Collaboration, Felix AHARONIAN,¹ Hiroki AKAMATSU,²
Fumie AKIMOTO,³ Steven W. ALLEN,^{4,5,6} Lorella ANGELINI,⁷ Marc AUDARD,⁸
Hisamitsu AWAKI,⁹ Magnus AXELSSON,¹⁰ Aya BAMBA,^{11,12}
Marshall W. BAUTZ,¹³ Roger BLANDFORD,^{4,5,6} Laura W. BRENNEMAN,¹⁴
Gregory V. BROWN,¹⁵ Esra BULBUL,¹³ Edward M. CACKETT,¹⁶
Maria CHERNYAKOVA,¹ Meng P. CHIAO,⁷ Paolo S. COPPI,^{17,18} Elisa COSTANTINI,²
Jelle DE PLAA,² Cor P. DE VRIES,² Jan-Willem DEN HERDER,² Chris DONE,¹⁹
Tadayasu DOTANI,²⁰ Ken EBISAWA,²⁰ Megan E. ECKART,⁷ Teruaki ENOTO,^{21,22}
Yuichiro EZOE,²³ Andrew C. FABIAN,²⁴ Carlo FERRIGNO,⁸ Adam R. FOSTER,¹⁴
Ryuichi FUJIMOTO,²⁵ Yasushi FUKAZAWA,²⁶ Akihiro FURUZAWA,²⁷
Massimiliano GALEAZZI,²⁸ Luigi C. GALLO,²⁹ Poshak GANDHI,³⁰
Margherita GIUSTINI,² Andrea GOLDWURM,^{31,32} Liyi GU,² Matteo GUAINAZZI,³³
Yoshito HABA,³⁴ Kouichi HAGINO,²⁰ Kenji HAMAGUCHI,^{7,35} Ilana M. HARRUS,^{7,35}
Isamu HATSUKADE,³⁶ Katsuhiko HAYASHI,²⁰ Takayuki HAYASHI,³⁷
Kiyoshi HAYASHIDA,³⁸ Junko S. HIRAGA,³⁹ Ann HORNSCHMEIER,⁷
Akio HOSHINO,⁴⁰ John P. HUGHES,⁴¹ Yuto ICHINOHE,²³ Ryo IZUKA,²⁰
Hajime INOUE,⁴² Yoshiyuki INOUE,²⁰ Manabu ISHIDA,²⁰ Kumi ISHIKAWA,²⁰
Yoshitaka ISHISAKI,²³ Masachika IWAI,²⁰ Jelle KAASTRA,^{2,43} Tim KALLMAN,⁷
Tsuneyoshi KAMAE,¹¹ Jun KATAOKA,⁴⁴ Satoru KATSUDA,⁴⁵ Nobuyuki KAWAI,⁴⁶
Richard L. KELLEY,⁷ Caroline A. KILBOURNE,⁷ Takao KITAGUCHI,²⁶
Shunji KITAMOTO,⁴⁰ Tetsu KITAYAMA,⁴⁷ Takayoshi KOHMURA,⁴⁸
Motohide KOKUBUN,²⁰ Katsuji KOYAMA,⁴⁹ Shu KOYAMA,²⁰
Peter KRETSCHMAR,⁵⁰ Hans A. KRIMM,^{51,52} Aya KUBOTA,⁵³ Hideyo KUNIEDA,³⁷
Philippe LAURENT,^{31,32} Shiu-Hang LEE,²¹ Maurice A. LEUTENEGGER,⁷
Olivier O. LIMOUSIN,³² Michael LOEWENSTEIN,⁷ Knox S. LONG,⁵⁴ David LUMB,³³
Greg MADEJSKI,⁴ Yoshitomo MAEDA,²⁰ Daniel MAIER,^{31,32} Kazuo MAKISHIMA,⁵⁵
Maxim MARKEVITCH,⁷ Hironori MATSUMOTO,³⁸ Kyoko MATSUSHITA,⁵⁶
Dan MCCAMMON,⁵⁷ Brian R. McNAMARA,⁵⁸ Missagh MEHDIPOUR,²
Eric D. MILLER,¹³ Jon M. MILLER,⁵⁹ Shin MINESHIGE,²¹ Kazuhisa MITSUDA,²⁰
Ikuyuki MITSUISHI,³⁷ Takuya MIYAZAWA,⁶⁰ Tsunefumi MIZUNO,²⁶
Hideyuki MORI,⁷ Koji MORI,³⁶ Koji MUKAI,^{7,35} Hiroshi MURAKAMI,⁶¹
Richard F. MUSHOTZKY,⁶² Takao NAKAGAWA,²⁰ Hiroshi NAKAJIMA,^{38,†}
Takeshi NAKAMORI,⁶³ Shinya NAKASHIMA,⁵⁵ Kazuhiro NAKAZAWA,¹¹
Kumiko K. NOBUKAWA,⁶⁴ Masayoshi NOBUKAWA,⁶⁵ Hirofumi NODA,^{66,67}
Hirokazu ODAKA,⁴ Takaya OHASHI,²³ Masanori OHNO,²⁶ Takashi OKAJIMA,⁷
Naomi OTA,⁶⁴ Masanobu OZAKI,²⁰ Frits PAERELS,⁶⁸ Stéphane PALTANI,⁸

Robert PETRE,⁷ **Ciro PINTO**,²⁴ **Frederick S. PORTER**,⁷ **Katja POTTSCHMIDT**,^{7,35}
Christopher S. REYNOLDS,⁶² **Samar SAFI-HARB**,⁶⁹ **Shinya SAITO**,⁴⁰
Kazuhiro SAKAI,⁷ **Toru SASAKI**,⁵⁶ **Goro SATO**,²⁰ **Kosuke SATO**,⁵⁶ **Rie SATO**,²⁰
Makoto SAWADA,⁷⁰ **Norbert SCHARTEL**,⁵⁰ **Peter J. SERLEMTSOS**,⁷
Hiromi SETA,²³ **Megumi SHIDATSU**,⁵⁵ **Aurora SIMIONESCU**,²⁰
Randall K. SMITH,¹⁴ **Yang SOONG**,⁷ **Łukasz STAWARZ**,⁷¹ **Yasuharu SUGAWARA**,²⁰
Satoshi SUGITA,⁴⁶ **Andrew SZYMKOWIAK**,¹⁷ **Hiroyasu TAJIMA**,³
Hiromitsu TAKAHASHI,²⁶ **Tadayuki TAKAHASHI**,²⁰ **Shiníchihiro TAKEDA**,⁶⁰
Yoh TAKEI,²⁰ **Toru TAMAGAWA**,⁵⁵ **Takayuki TAMURA**,²⁰ **Takaaki TANAKA**,⁴⁹
Yasuo TANAKA,⁷² **Yasuyuki T. TANAKA**,²⁶ **Makoto S. TASHIRO**,⁷³
Yuzuru TAWARA,³⁷ **Yukikatsu TERADA**,⁷³ **Yuichi TERASHIMA**,⁹
Francesco TOMBESI,^{7,62} **Hiroshi TOMIDA**,²⁰ **Yohko TSUBOI**,⁴⁵
Masahiro TSUJIMOTO,²⁰ **Hiroshi TSUNEMI**,³⁸ **Takeshi Go TSURU**,⁴⁹
Hiroyuki UCHIDA,⁴⁹ **Hideki UCHIYAMA**,⁷⁴ **Yasunobu UCHIYAMA**,⁴⁰
Shutaro UEDA,²⁰ **Yoshihiro UEDA**,²¹ **Shiníchihiro UNO**,⁷⁵ **C. Megan URRY**,¹⁷
Eugenio URSINO,²⁸ **Shin WATANABE**,²⁰ **Norbert WERNER**,^{76,77,26}
Dan R. WILKINS,⁴ **Brian J. WILLIAMS**,⁵⁴ **Shinya YAMADA**,²³ **Hiroya YAMAGUCHI**,⁷
Kazutaka YAMAOKA,³ **Noriko Y. YAMASAKI**,²⁰ **Makoto YAMAUCHI**,³⁶
Shigeo YAMAUCHI,⁶⁴ **Tahir YAQOUB**,³⁵ **Yoichi YATSU**,⁴⁶ **Daisuke YONETOKU**,²⁵
Irina ZHURAVLEVA,^{4,5} **Abderahmen ZOGHBI**,⁵⁹ and **Nozomi NAKANIWA**²⁰

¹Dublin Institute for Advanced Studies, 31 Fitzwilliam Place, Dublin 2, Ireland

²SRON Netherlands Institute for Space Research, Sorbonnelaan 2, 3584 CA Utrecht, The Netherlands

³Institute for Space-Earth Environmental Research, Nagoya University, Furo-cho, Chikusa-ku, Nagoya, Aichi 464-8601, Japan

⁴Kavli Institute for Particle Astrophysics and Cosmology, Stanford University, 452 Lomita Mall, Stanford, CA 94305, USA

⁵Department of Physics, Stanford University, 382 Via Pueblo Mall, Stanford, CA 94305, USA

⁶SLAC National Accelerator Laboratory, 2575 Sand Hill Road, Menlo Park, CA 94025, USA

⁷NASA, Goddard Space Flight Center, 8800 Greenbelt Road, Greenbelt, MD 20771, USA

⁸Department of Astronomy, University of Geneva, ch. d'Écogia 16, CH-1290 Versoix, Switzerland

⁹Department of Physics, Ehime University, 2-5 Bunkyo-cho, Matsuyama, Ehime 790-8577, Japan

¹⁰Department of Physics and Oskar Klein Center, Stockholm University, 106 91 Stockholm, Sweden

¹¹Department of Physics, The University of Tokyo, 7-3-1 Hongo, Bunkyo-ku, Tokyo 113-0033, Japan

¹²Research Center for the Early Universe, School of Science, The University of Tokyo, 7-3-1 Hongo, Bunkyo-ku, Tokyo 113-0033, Japan

¹³Kavli Institute for Astrophysics and Space Research, Massachusetts Institute of Technology, 77 Massachusetts Avenue, Cambridge, MA 02139, USA

¹⁴Harvard-Smithsonian Center for Astrophysics, 60 Garden Street, Cambridge, MA 02138, USA

¹⁵Lawrence Livermore National Laboratory, 7000 East Avenue, Livermore, CA 94550, USA

¹⁶Department of Physics and Astronomy, Wayne State University, 666 W. Hancock St, Detroit, MI 48201, USA

¹⁷Department of Physics, Yale University, New Haven, CT 06520-8120, USA

¹⁸Department of Astronomy, Yale University, New Haven, CT 06520-8101, USA

¹⁹Centre for Extragalactic Astronomy, Department of Physics, University of Durham, South Road, Durham, DH1 3LE, UK

²⁰Japan Aerospace Exploration Agency, Institute of Space and Astronautical Science, 3-1-1 Yoshino-dai, Chuo-ku, Sagami-hara, Kanagawa 252-5210, Japan

- ²¹Department of Astronomy, Kyoto University, Kitashirakawa-Oiwake-cho, Sakyo-ku, Kyoto, Kyoto 606-8502, Japan
- ²²The Hakubi Center for Advanced Research, Kyoto University, Yoshida-honmachi, Sakyo-ku, Kyoto, Kyoto 606-8501, Japan
- ²³Department of Physics, Tokyo Metropolitan University, 1-1 Minami-Osawa, Hachioji, Tokyo 192-0397, Japan
- ²⁴Institute of Astronomy, University of Cambridge, Madingley Road, Cambridge, CB3 0HA, UK
- ²⁵Faculty of Mathematics and Physics, Kanazawa University, Kakuma-machi, Kanazawa, Ishikawa 920-1192, Japan
- ²⁶School of Science, Hiroshima University, 1-3-1 Kagamiyama, Higashi-Hiroshima, Hiroshima 739-8526, Japan
- ²⁷Fujita Health University, 1-98 Dengakugakubo, Kutsukake-cho, Toyoake, Aichi 470-1192, Japan
- ²⁸Physics Department, University of Miami, 1320 Campo Sano Dr., Coral Gables, FL 33146, USA
- ²⁹Department of Astronomy and Physics, Saint Mary's University, 923 Robie Street, Halifax, NS, B3H 3C3, Canada
- ³⁰Department of Physics and Astronomy, University of Southampton, Highfield, Southampton, SO17 1BJ, UK
- ³¹Laboratoire APC, 10 rue Alice Domon et Léonie Duquet, 75013 Paris, France
- ³²CEA Saclay, 91191 Gif sur Yvette, France
- ³³European Space Research and Technology Center, Keplerlaan 1, 2201 AZ Noordwijk, The Netherlands
- ³⁴Department of Physics and Astronomy, Aichi University of Education, 1 Hirosawa, Igaya-cho, Kariya, Aichi 448-8543, Japan
- ³⁵Department of Physics, University of Maryland Baltimore County, 1000 Hilltop Circle, Baltimore, MD 21250, USA
- ³⁶Department of Applied Physics and Electronic Engineering, University of Miyazaki, 1-1 Gakuen Kibanadai-Nishi, Miyazaki, Miyazaki 889-2192, Japan
- ³⁷Department of Physics, Nagoya University, Furo-cho, Chikusa-ku, Nagoya, Aichi 464-8602, Japan
- ³⁸Department of Earth and Space Science, Osaka University, 1-1 Machikaneyama-cho, Toyonaka, Osaka 560-0043, Japan
- ³⁹Department of Physics, Kwansei Gakuin University, 2-1 Gakuen, Sanda, Hyogo 669-1337, Japan
- ⁴⁰Department of Physics, Rikkyo University, 3-34-1 Nishi-Ikebukuro, Toshima-ku, Tokyo 171-8501, Japan
- ⁴¹Department of Physics and Astronomy, Rutgers University, 136 Frelinghuysen Road, Piscataway, NJ 08854, USA
- ⁴²Meisei University, 2-1-1 Hodokubo, Hino, Tokyo 191-8506, Japan
- ⁴³Leiden Observatory, Leiden University, PO Box 9513, 2300 RA Leiden, The Netherlands
- ⁴⁴Research Institute for Science and Engineering, Waseda University, 3-4-1 Ohkubo, Shinjuku-ku, Tokyo 169-8555, Japan
- ⁴⁵Department of Physics, Chuo University, 1-13-27 Kasuga, Bunkyo-ku, Tokyo 112-8551, Japan
- ⁴⁶Department of Physics, Tokyo Institute of Technology, 2-12-1 Ookayama, Meguro-ku, Tokyo 152-8550, Japan
- ⁴⁷Department of Physics, Toho University, 2-2-1 Miyama, Funabashi, Chiba 274-8510, Japan
- ⁴⁸Department of Physics, Tokyo University of Science, 2641 Yamazaki, Noda, Chiba 278-8510, Japan
- ⁴⁹Department of Physics, Kyoto University, Kitashirakawa-Oiwake-cho, Sakyo-ku, Kyoto, Kyoto 606-8502, Japan
- ⁵⁰European Space Astronomy Center, Camino Bajo del Castillo, s/n., 28692 Villanueva de la Cañada, Madrid, Spain
- ⁵¹Universities Space Research Association, 7178 Columbia Gateway Drive, Columbia, MD 21046, USA
- ⁵²National Science Foundation, 4201 Wilson Blvd, Arlington, VA 22230, USA
- ⁵³Department of Electronic Information Systems, Shibaura Institute of Technology, 307 Fukasaku, Minuma-ku, Saitama, Saitama 337-8570, Japan
- ⁵⁴Space Telescope Science Institute, 3700 San Martin Drive, Baltimore, MD 21218, USA

- ⁵⁵Institute of Physical and Chemical Research, 2-1 Hirosawa, Wako, Saitama 351-0198, Japan
- ⁵⁶Department of Physics, Tokyo University of Science, 1-3 Kagurazaka, Shinjuku-ku, Tokyo 162-8601, Japan
- ⁵⁷Department of Physics, University of Wisconsin, Madison, WI 53706, USA
- ⁵⁸Department of Physics and Astronomy, University of Waterloo, 200 University Avenue West, Waterloo, Ontario, N2L 3G1, Canada
- ⁵⁹Department of Astronomy, University of Michigan, 1085 South University Avenue, Ann Arbor, MI 48109, USA
- ⁶⁰Okinawa Institute of Science and Technology Graduate University, 1919-1 Tancha, Onna-son, Kunigami-gun, Okinawa 904-0495, Japan
- ⁶¹Faculty of Liberal Arts, Tohoku Gakuin University, 2-1-1 Tenjinzawa, Izumi-ku, Sendai, Miyagi 981-3193, Japan
- ⁶²Department of Astronomy, University of Maryland, College Park, MD 20742, USA
- ⁶³Faculty of Science, Yamagata University, 1-4-12 Kojirakawa-machi, Yamagata, Yamagata 990-8560, Japan
- ⁶⁴Department of Physics, Nara Women's University, Kitauoyanishi-machi, Nara, Nara 630-8506, Japan
- ⁶⁵Department of Teacher Training and School Education, Nara University of Education, Takabatake-cho, Nara, Nara 630-8528, Japan
- ⁶⁶Frontier Research Institute for Interdisciplinary Sciences, Tohoku University, 6-3 Aramaki-aza-aoba, Aoba-ku, Sendai, Miyagi 980-8578, Japan
- ⁶⁷Astronomical Institute, Tohoku University, 6-3 Aramakiazaoaoba, Aoba-ku, Sendai, Miyagi 980-8578, Japan
- ⁶⁸Astrophysics Laboratory, Columbia University, 550 West 120th Street, New York, NY 10027, USA
- ⁶⁹Department of Physics and Astronomy, University of Manitoba, Winnipeg, MB R3T 2N2, Canada
- ⁷⁰Department of Physics and Mathematics, Aoyama Gakuin University, 5-10-1 Fuchinobe, Chuo-ku, Sagami-hara, Kanagawa 252-5258, Japan
- ⁷¹Astronomical Observatory of Jagiellonian University, ul. Orla 171, 30-244 Kraków, Poland
- ⁷²Max Planck Institute for extraterrestrial Physics, Giessenbachstrasse 1, 85748 Garching, Germany
- ⁷³Department of Physics, Saitama University, 255 Shimo-Okubo, Sakura-ku, Saitama, Saitama 338-8570, Japan
- ⁷⁴Faculty of Education, Shizuoka University, 836 Ohya, Suruga-ku, Shizuoka, Shizuoka 422-8529, Japan
- ⁷⁵Faculty of Health Sciences, Nihon Fukushi University, 26-2 Higashi Haemi-cho, Handa, Aichi 475-0012, Japan
- ⁷⁶MTA-Eötvös University Lendület Hot Universe Research Group, Pázmány Péter sétány 1/A, Budapest, 1117, Hungary
- ⁷⁷Department of Theoretical Physics and Astrophysics, Faculty of Science, Masaryk University, Kotlářská 2, Brno, 602 00, Czech Republic

*The corresponding authors are Hiroshi Nakajima, Kiyoshi Hayashida, Tim Kallman, Takuya Miyazawa, Hiromitsu Takahashi, and Matteo Guainazzi.

†E-mail: nakajima@ess.sci.osaka-u.ac.jp

Received 2017 August 26; Accepted 2017 November 21

Abstract

We report on a Hitomi observation of IGR J16318–4848, a high-mass X-ray binary system with an extremely strong absorption of $N_{\mathrm{H}} \sim 10^{24} \mathrm{cm}^{-2}$. Previous X-ray studies revealed that its spectrum is dominated by strong fluorescence lines of Fe as well as continuum emission lines. For physical and geometrical insight into the nature of the reprocessing material, we utilized the high spectroscopic resolving power of the X-ray microcalorimeter (the soft X-ray spectrometer: SXS) and the wide-band sensitivity by the soft and hard X-ray imagers (SXI and HXI) aboard Hitomi. Even though the photon counts are limited due to unintended off-axis pointing, the SXS spectrum resolves Fe

$K\alpha_1$ and $K\alpha_2$ lines and puts strong constraints on the line centroid and line width. The line width corresponds to a velocity of 160^{+300}_{-70} km s $^{-1}$. This represents the most accurate, and smallest, width measurement of this line made so far from the any X-ray binary, much less than the Doppler broadening and Doppler shift expected from speeds that are characteristic of similar systems. Combined with the K-shell edge energy measured by the SXI and HXI spectra, the ionization state of Fe is estimated to be in the range of Fe I–IV. Considering the estimated ionization parameter and the distance between the X-ray source and the absorber, the density and thickness of the materials are estimated. The extraordinarily strong absorption and the absence of a Compton shoulder component have been confirmed. These characteristics suggest reprocessing materials that are distributed in a narrow solid angle or scattering, primarily by warm free electrons or neutral hydrogen. This measurement was achieved using the SXS detection of 19 photons. It provides strong motivation for follow-up observations of this and other X-ray binaries using the X-ray Astrophysics Recovery Mission and other comparable future instruments.

Key words: binaries: general — stars: individual (IGR J16318–4848) — X-rays: binaries

1 Introduction

High-mass X-ray binaries (HMXBs) consist of a compact object (neutron star or black hole candidate) and a massive companion star that is typically a Be star or a supergiant O- or B-type star. HMXBs with a Be companion often show periodic variability in X-ray flux when the compact object passes through a circumstellar decretion disk surrounding the star. Supergiant HMXBs exhibit X-ray time variability associated with an eclipse, or partial eclipse, of the compact object by the companion star.

In addition to the comprehensive catalog of the galactic HMXBs by Liu et al. (2006), a recent deep survey in the hard X-ray and soft gamma-ray bands, performed by IBIS/ISGRI (Ubertini et al. 2003; Lebrun et al. 2003), on board International Gamma-Ray Astrophysics Laboratory (INTEGRAL) (Winkler et al. 2003) has discovered a considerable number of HMXBs, which are summarized in a catalog by Krivonos et al. (2017). More than half of these exhibit persistent time variability in the hard X-ray band (Lutovinov et al. 2013). One of the highlights of the survey is the discovery of a number of HMXBs that exhibit extraordinarily strong absorption with their distribution in the galaxy correlating with that of star-forming regions (Bodaghee et al. 2012; Coleiro & Chaty 2013). IGR J16318–4848 (hereafter IGR J16318) was first discovered, and remains the most extreme example of such objects.

IGR J16318 was discovered in a scanning observation of the Galactic plane by the INTEGRAL/IBIS/ISGRI (Courvoisier et al. 2003; Walter et al. 2003). An examination of archival ASCA data revealed extremely strong X-ray absorption in the direction of the source (Murakami et al. 2003). The X-ray spectrum is dominated by Fe $K\alpha$, $K\beta$, and

Ni $K\alpha$ fluorescence emission lines and a continuum (Matt & Guainazzi 2003; Revnivtsev 2003). The fluorescence lines as well as the continuum vary on time scales of thousands of seconds, corresponding to an upper limit on the emitting region size of approximately 10^{13} cm (Walter et al. 2003).

The optical/near-infrared (NIR) counterpart exhibits less absorption than that measured in the X-ray band, which implies that the absorbing material is concentrated around the compact object (Filliatre & Chaty 2004; Lutovinov et al. 2005). NIR spectroscopy suggests that the counterpart is a supergiant B[e] star (Filliatre & Chaty 2004), based on the detection of forbidden lines of Fe. Such stars are also known to contain dust in their envelopes (Miroshnichenko 2007); a mid-infrared observation revealed that it is surrounded by dust and cold gas with a heated inner rim (Chaty & Rahoui 2012). The distance to the target was derived by Filliatre and Chaty (2004), based on a fitting of the optical/NIR spectral energy distribution (SED) to be 0.9–6.2 kpc. Rahoui et al. (2008) performed an SED fitting from the optical to mid-infrared band, and obtained a distance of 1.6 kpc, utilizing the known stellar classification of the companion star.

Long-term monitoring of the hard X-ray flux with Swift/BAT shows a periodicity of ~ 80 d (Jain et al. 2009; Iyer & Paul 2017). Although the companion star belongs to the spectral type of B[e], there is no obvious coincidence between the numbers of outbursts and the orbital phase (Jain et al. 2009). Monitoring in the soft and hard X-ray bands shows that the source is always bright with a flux dynamic range of a factor 5 and Compton thick ($N_H \geq 1.1 \times 10^{24}$ cm $^{-2}$) (Barragan et al. 2010). The statistically best spectrum obtained with Suzaku (Mitsuda et al. 2007) shows no Compton shoulder, which implies a non-spherical

and inhomogeneous absorber (Barragán et al. 2009). The average X-ray spectrum of the source exhibits a continuum typical for neutron stars (Walter et al. 2004). Moreover, the source shows a disagreement in its X-ray/radio flux relationship with that observed in the low/hard state of black-hole binaries (Filliatre & Chaty 2004). Nevertheless, the nature of the compact source (neutron star or black hole candidate) is uncertain because pulsations have not been detected.

Hitomi, the Japan-led X-ray astronomy satellite (Takahashi et al. 2018), carried a microcalorimeter array (SXS: soft X-ray spectrometer) (Kelley et al. 2018), which had outstanding energy resolution in the energy band containing the Fe K-shell lines. Combined with an X-ray CCD camera (SXI: soft X-ray imager) (Tanaka et al. 2018) and a hard X-ray imager (HXI) (Nakazawa et al. 2018), it provided unprecedented wide-band imaging spectroscopy. Hitomi was lost due to an accident one month after the launch. The observation of IGR J16318 was performed during the instrument check-out phase to demonstrate the spectroscopic performance of Hitomi. In spite of offset pointing during the observation, due to incomplete attitude calibration, it is possible to extract significant scientific results from the limited data.

In the remainder of this paper, we first describe the observation log, including some notes on the data reduction in section 2. The imaging and spectroscopic analyses (section 3) are followed by the discussion (section 4) and summary (section 5). Measurement errors correspond to the 90% confidence level, unless otherwise indicated.

2 Observation and data reduction

2.1 Observation

Pointing toward IGR J16318 started on 2016 March 10, 22:28 UT and ended on 2016 March 14, 16:20 UT. While the SXS and SXI were already in operation, the HXI was undergoing the startup procedure of one of the two sensors (HXI-1). Because the observation was performed before optimizing the alignment matrices of star trackers (STT1 and STT2), the target was at off-axis positions throughout the observation. The off-axis angle was $5'$ according to the SXI image after a switch of the STT from STT1 to STT2 on March 13, 17:58, which limited the effective area of all instruments. The fields of view (FoV) of the SXS and HXI are $3'.05$ by $3'.05$ and $9'.2$ by $9'.2$ squares, respectively. Therefore, only the SXI caught the target securely within its FoV, thanks to its large FoV of $38'$ by $38'$ square (Nakajima 2018).

The microcalorimeter array in the SXS was already in thermal equilibrium at the time of our observation

(Fujimoto et al. 2016; Noda et al. 2016). The energy resolution of the onboard radioactive ^{55}Fe source was 4.9 eV full width half maximum (FWHM), as reported by A. M. Leutenegger et al. (in preparation). However, the SXS was not in the normal operation mode in terms of some calibration items as follows. The gate valve was still closed, and hence the effective area in the soft energy band was limited. The Modulated X-ray Source (MXS: de Vries et al. 2018) was also not yet available for contemporaneous gain measurements, which forced us to estimate the gain uncertainty only by onboard radioactive ^{55}Fe sources.

The SXI was in normal operation with the “Full Window + No Burst” mode (Tanaka et al. 2018). The temperature of CCDs was already stable at -110°C at the time of the exposure (Nakajima et al. 2018). The observation was carried out before optimizing the parameters for the dark-level calculation, and hence the SXI suffered from a cross-talk issue. That is, an anomalously low dark level can be induced in a pixel by a charged-particle event in the adjacent segment. The dark level leads to continuous false events in the pixel, and the erroneously higher pulse heights for the normal events around the pixel. To minimize the effect of the cross-talk issue, the lower threshold of the effective energy band was set to be 100 ch, which corresponds to 600 eV.

HXI-1 completed its startup procedure and started observation on March 12, 21:30 UT. The target came at the edge of the HXI-1 FoV after the switch of the STT. Another sensor, HXI-2, was still undergoing increasing of the high voltage for the Si/CdTe double-sided strip detectors.

2.2 Data reduction

Hereafter, we concentrate on the data after the STT switch because event files of all three instruments are available in the interval. We utilize the data cleaned and processed with a script version 03.01.005.005. All of the reduction and analyses described below employed the Hitomi software version 5b and the calibration database released on 2017 May 11 (Angelini et al. 2018).¹ The effective exposure times of the SXI, SXS, and HXI-1 are 39.4, 68.9, and 39.4 ks, respectively, after the data reduction.

2.2.1 SXS

Owing to the shape of the point spread function (PSF) of the soft X-ray telescope (SXT-S: Maeda et al. 2018), some photons from the target reached the SXS in spite of the off-axis pointing. Furthermore, there was a wobble of the satellite at the beginning of the observation, so that the

¹ (<https://heasarc.gsfc.nasa.gov/docs/hitomi/calib/>).

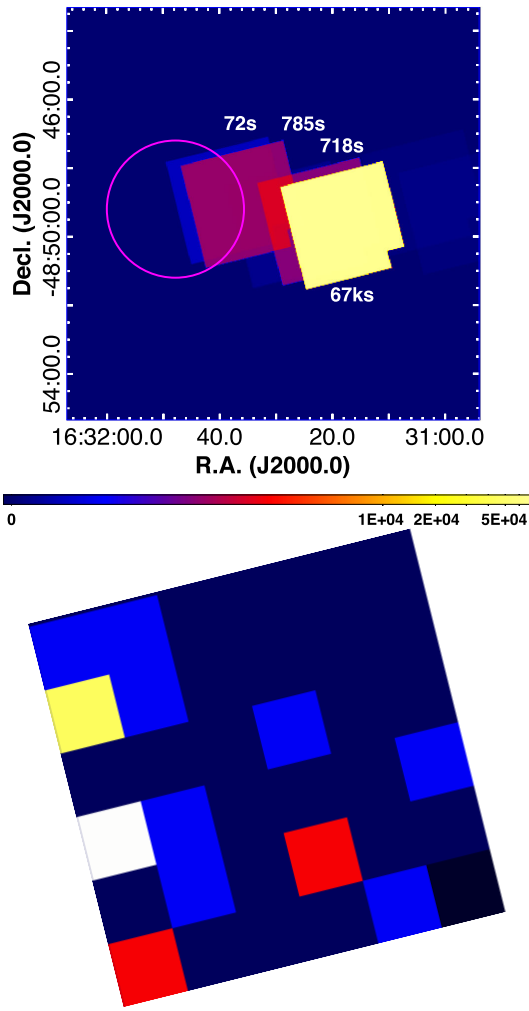


Fig. 1. Top: SXS exposure map with the designation of the exposure time for each pointing position. The magenta circle corresponds to the source extraction region for the SXS (see figure 4 bottom panel). Bottom: Spatial event distribution of the SXS microcalorimeter array in the DET coordinate in the energy band from 6.38 to 6.42 keV. Blue, red, yellow, and white pixels correspond to detections of one, two, three, and four events, respectively. The black pixel at the bottom right is the calibration pixel that is not directly exposed to the sky. (Color online)

optical axis of the SXT-S temporarily approached the target direction. Then, a part of the FoV of the SXS overlapped with a photon-extracting region for the SXS, as shown in figure 1, top panel.

To retrieve photons from the target during the wobbling, we relaxed the standard screening criteria for the angular distance between the actual pointing and the mean pointing position (ANG_DIST) from 1.5 to 4.0. Besides the grade filtering in the standard screening, events flagged due to close proximity in time of 0.72 ms to other events are additionally filtered.

Figure 2 shows light curves around the Fe K α line, a wide energy band as well as the history of the ANG_DIST. The events are concentrated around the time of the wobbling

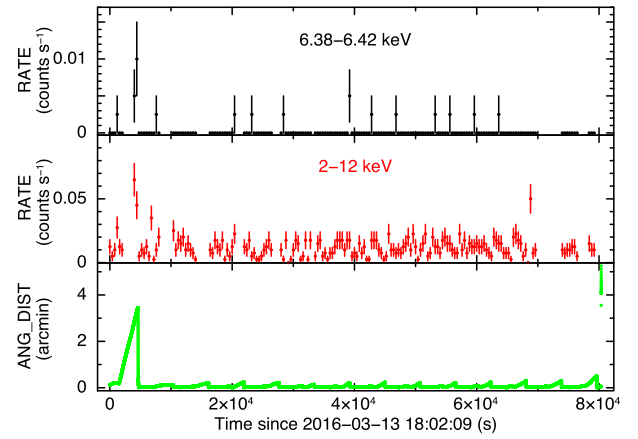


Fig. 2. Top: Event light curve of the SXS full array in the energy band from 6.38 to 6.42 keV binned with 400 s. Middle: Same as the top panel but for the wide energy band from 2 to 12 keV. Bottom: History of ANG_DIST with 8 s resolution. (Color online)

in both energy bands. There is no bright celestial target in the direction where the satellite pointed at this time. No background flare events can be seen for other instruments around this time. Figure 1, bottom panel, shows the spatial distribution of the events in the energy band from 6.38 to 6.42 keV. The 19 events spatially concentrate toward the target position. This provides a strong indication that these events originated from the target.

2.2.2 SXS and HXI

With regard to the SXS data, false events originating from the cross-talk issue are eliminated with the parameters in `sxipeline` set as follows: N_{\min} of 6, PHA_{sp} of 15, and R of 0.7 (Nakajima et al. 2018). The SXS also suffers from a light leak due to optical/infrared light primarily when the minus Z axis of the spacecraft points to the day earth (MZDYE). Although our observation was free from the MZDYE periods, there was another moderate light leak during the sun illumination of the spacecraft. We also see possible charges left inside the CCDs after the passage of the South Atlantic Anomaly (SAA) as described in Nakajima et al. (2018). The pulse heights of the events detected around the physical edge of the CCDs are weakly affected by these issues. The target was always near the physical edge of the CCD1 during the exposure. To minimize the effect of these problems, we choose only data during the eclipse of the spacecraft, and when the time after the passage of the SAA is larger than 1800 s (Nakajima et al. 2018). The pile-up fraction is estimated using `pileest` and the results is below 0.7% with a grade migration parameter of 0.1.

No additional filtering is applied to the HXI-1 cleaned event files.

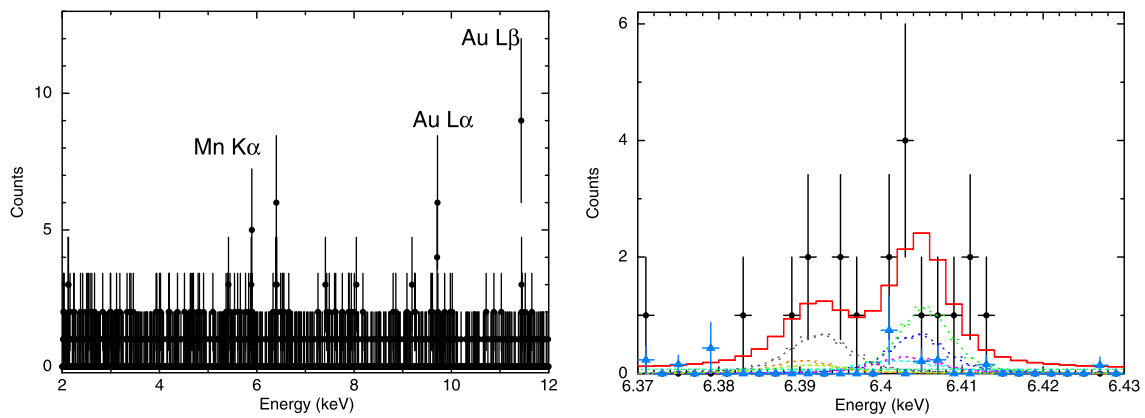


Fig. 3. Left: SXS spectrum summed up on all the 35 pixels. Peaks around 5.9, 9.7, and 11.5 keV are the instrumental backgrounds of Mn $K\alpha$, Au $L\alpha$, and Au $L\beta$, respectively. Poisson error bars (Gehrels 1986) are presented. Note that the spectrum is binned to 4 eV. Right: Same as the left-hand panel but for the energy range near 6.4 keV. The sum of the fitted models of seven Lorentzian functions for the Fe $K\alpha$ lines and a power-law is shown in a solid red line, with each component shown in dashed lines and different colors. Although the fitting is performed using the original 0.5 eV per bin spectrum, we show the spectrum with a binning of 2 eV for display purposes. Blue data with filled triangles are the calculated NXB spectrum that is not subtracted from the source spectrum. (Color online)

3 Analyses

All of the spectral analyses described below were performed using XSPEC v12.9.0u (Arnaud 1996). We adopted the spectral model `tbvarabs` for the photoelectric absorption using the interstellar medium abundances described in Wilms et al. (2000).

3.1 SXS spectral analysis

The spectrum obtained with the SXS in the 2–12 keV band is shown in the left-hand panel of figure 3. The events are summed over all the 35 pixels and their total number is 752. The concentrations of events near 5.9, 9.7, and 11.5 keV originated from the instrumental background lines of Mn $K\alpha$, Au $L\alpha$, and Au $L\beta$, respectively. Due to the limited statistics of the events, we focused on the spectral analysis around a peak at 6.4 keV, which is magnified in the right-hand panel of figure 3. Most of the events fall within 6.39–6.41 keV, and the primary peak is slightly above 6.40 keV. This distribution corresponds to the Fe $K\alpha_1$ and $K\alpha_2$ lines.

We estimate the number of non-X-ray background (NXB) events (Kilbourne et al. 2018) included in the 6.4 keV line utilizing `sxsnxbgen`. This tool considers the magnetic cut-off rigidity (COR) weighting of the observation and extract events with the identical filtering with the source data from the SXS archive NXB event file. Because the events in the energy band of 6.38–6.42 keV are detected in the specific pixels, as shown in the bottom panel of figure 1, we only consider those pixels to calculate the NXB. The estimated NXB spectrum is overlaid on the source spectrum in the right-hand panel of figure 3.

The expected number of NXB counts in the 6.38–6.42 keV range is ≤ 2 when we assume the same exposure time as on the target.

The $K\alpha$ line centroid near 6.4 keV implies a neutral or near-neutral ionization state of Fe. If so, the line should be modeled with Lorentzian functions (Agarwal 1979) that analytically represent the natural shape of an emission line. It is well known that the $K\alpha$ lines of the 3d transition metals are highly asymmetric. Hölzer et al. (1997) applied seven Lorentzians to accurately represent the asymmetric $K\alpha$ line from neutral Fe. We assumed the near-neutral state and then adopted the best-fit parameters in Hölzer et al. (1997), which are justified in section 4. The NXB spectrum is represented using a power-law model with its index fixed to zero. The power-law component is also included in the source spectrum with its parameters linked between the source and the background. We set the following four parameters to be free: the energy at the maximum of the primary Lorentzian (α_{11} in table II in Hölzer et al. 1997), its width, the normalization factor by which all the seven Lorentzians are commonly multiplied, and the flux of the power-law component. The relative energy at the maximum of each Lorentzian is fixed as well as the relative width and amplitude. The continuum emissions from the target and the cosmic X-ray background are ignored from the statistical point of view. We adopt the C-statistic (Cash 1979) for the spectral fitting. The original 0.5 eV per bin source and background spectra are fitted while the binned spectra are shown in figure 3 for display purposes. The best-fit energy at the maximum of the primary Lorentzian is 6405.4 eV and its width is 3.5 eV (FWHM). This yields the Fe $K\alpha_1$ line centroid of 6404.3 eV, a value that is remarkably

Table 1. Best-fit parameters for the SXS spectrum.

Parameter	Value
$E_{\alpha 11}^*$ (eV)	6405.4 [†]
$\sigma_{\alpha 11}$ (FWHM in eV)	3.5 [†]
$I_{\alpha 11}$ ($10^{-4} \text{ cm}^{-2} \text{ s}^{-1}$)	2.4
Γ	0 (fixed)
A ($10^{-3} \text{ cm}^{-2} \text{ s}^{-1}$)	1.6
the C-statistic (d.o.f.)	131.7 (234)

*Energy at the maximum of the primary Lorentzian (α_{11} in table II in Hölzer et al. 1997).

[†]See text for a discussion of the probability distributions for $E_{\alpha 11}$ and $\sigma_{\alpha 11}$.

similar to that of neutral Fe (6403.1 eV) measured by Hölzer et al. (1997).

To investigate the probability distribution function in the parameter space, we performed Markov-chain Monte Carlo simulations within XSPEC. We adopted a proposal distribution of a Gaussian for the chain with a length of 10^5 . Considering the distribution, the energy at the maximum of the primary component and its width were estimated to be $6405.4^{+2.4}_{-2.5}$ eV and $3.5^{+6.4}_{-1.6}$ eV, respectively. The best-fit parameters for the spectral fit are summarized in table 1. This is the first observational result resolving Fe $K\alpha_1$ and Fe $K\alpha_2$ lines for X-ray binary systems, which demonstrates the superb energy resolution of the microcalorimeter.

The accuracy of the energy scale of the SXS is affected by the instrumental gain uncertainty. There had been no on-orbit full-array gain calibration before the observation of IGR J16318. A later calibration using the filter-wheel ^{55}Fe sources was carried out after changing several cooler power settings (M. E. Eckart et al. in preparation). Because the MXS was not yet available, a dedicated calibration pixel that was located outside of the aperture and continuously illuminated by a collimated ^{55}Fe source served as the only contemporaneous energy-scale reference. The time-dependent scaling required to correct the gain was applied to each pixel in the array. It was known, prior to launch, that the time-dependent gain-correction function for the calibration pixel generally did not adequately correct the energy scale of the array pixels. The relationship between changes of the calibration pixel and of the array was not fixed, but rather depended on the temperatures of the various shields and interfaces in the dewar. Therefore, although the relative drift rates across the array were characterized during the later calibration with the filter-wheel ^{55}Fe source, the changes in the cooler power settings between the IGR J16318 observation and its calibration limit the usefulness of that characterization. In fact, the measured relative gain drift predicts a much larger energy-scale offset between the final two pointings of the Perseus cluster of galaxies than that actually observed.

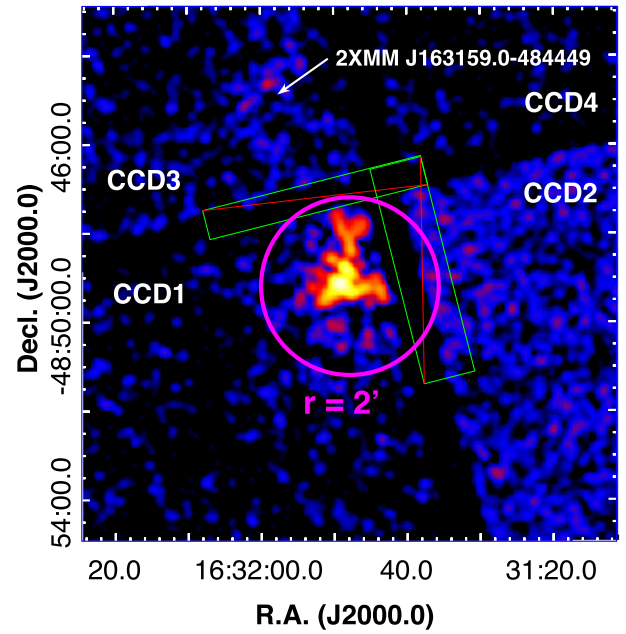


Fig. 4. SXI image in the energy band from 4.0 to 12 keV smoothed by a Gaussian of 6 pixels. Each CCD is designated together with a cataloged X-ray source. The source spectrum extraction region is shown with a magenta circle. Regions shown by green rectangles with red lines are excluded in the extraction. (Color online)

To overcome our limited ability to extrapolate from the calibration pixel, we examined the whole-array Mn $K\alpha$ instrumental line (Kilbourne et al. 2018) in source-free data taken from March 7 to March 15, when the SXS was being operated with the same cooler settings (Tsujiimoto et al. 2018) as those in the IGR J16318 observation. The SXS energy scale was found to be shifted by at most $+1 \pm 0.5$ eV at 5.9 keV. Further insight into the gain uncertainty comes from examining the errors in the Mn $K\beta$ position in the filter-wheel ^{55}Fe data after adjusting all of the pixels gain scales based on the Mn $K\alpha$ line. The errors ranged from -0.6 to $+0.2$ eV, which indicates the minimum scale of the gain uncertainty at 6.5 keV. We concluded that the gain shift with uncertainty of the line centroid of Fe $K\alpha$, which is between the Mn $K\alpha$ and Mn $K\beta$ lines, was $+1 \pm 0.5$ eV at the time of the observation of IGR J16318.

3.2 SXI and HXI analyses

The SXI image in the energy band from 4.0 to 12 keV is shown in figure 4. This shows the only additional X-ray source in the FoV, based on the 2XMMi-DR3 catalog (Lin et al. 2012). Note that the additional filtering of the sun illumination of the spacecraft and the time after the passage of the SAA was not applied to the image because the filtering has only a small effect on the pulse height of each event. Another note is that the PSF shape of the target

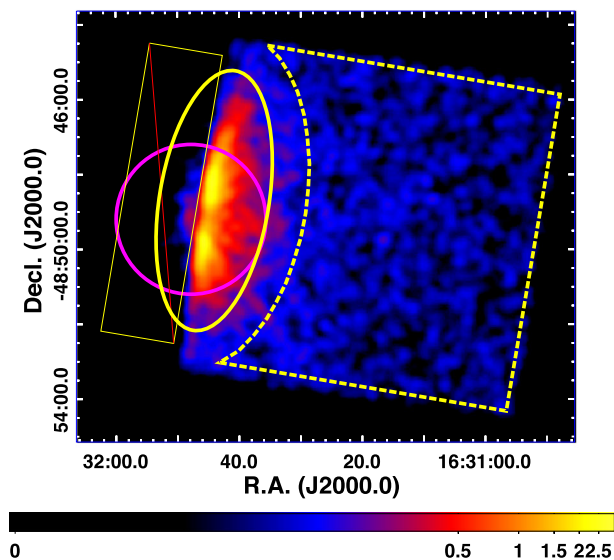


Fig. 5. HXI-1 image after standard screening in the energy band of 5.5 to 80 keV smoothed by a Gaussian of 8 pixels. Source and background regions are shown with a solid ellipse and a dashed polygon, respectively. The same sky region as that in figure 4 is designated with magenta circle for reference. A region shown by yellow rectangle with red line is excluded in the source extraction. (Color online)

is not smooth because some pixels are affected by the cross-talk issue (Nakajima et al. 2018), and have been filtered. In spite of the unintended off-axis pointing, the target was securely in the CCD1. A photon extracting region is drawn with a magenta circle.

The hard X-ray image obtained by the HXI-1 in the energy band from 5.5 to 80 keV is shown in figure 5. The circular region in magenta designates the same region as that in figure 4. Thanks to the moderate PSF of the hard X-ray telescope (Awaki et al. 2016), a number of events were detected even though the target was just on the edge of the FoV. The source and background spectra were extracted from the regions colored in yellow with solid and dashed lines, respectively.

Figure 6 shows light curves of SXI and HXI-1 extracted from the source regions designated in figure 4 and figure 5, respectively. Background was not subtracted and no aspect correction was applied. Barycenter and a dead-time correction were applied for the HXI-1 data prior to extraction. Note that the additional filtering of the sun illumination of the spacecraft and the time after the passage of the SAA was not applied for the SXI light curve because filtering has only a small effect on the pulse height of each event. The event rates in the energy band dominated by fluorescence lines and continuum both exhibit time variability on a time scale of thousands of seconds, which is also seen in the previous observations (Ibarra et al. 2007; Barragán et al. 2009). The root-mean-square fractional variation of the continuum band is 0.34 ± 0.03 (HXI-1) and < 0.17 (3σ)

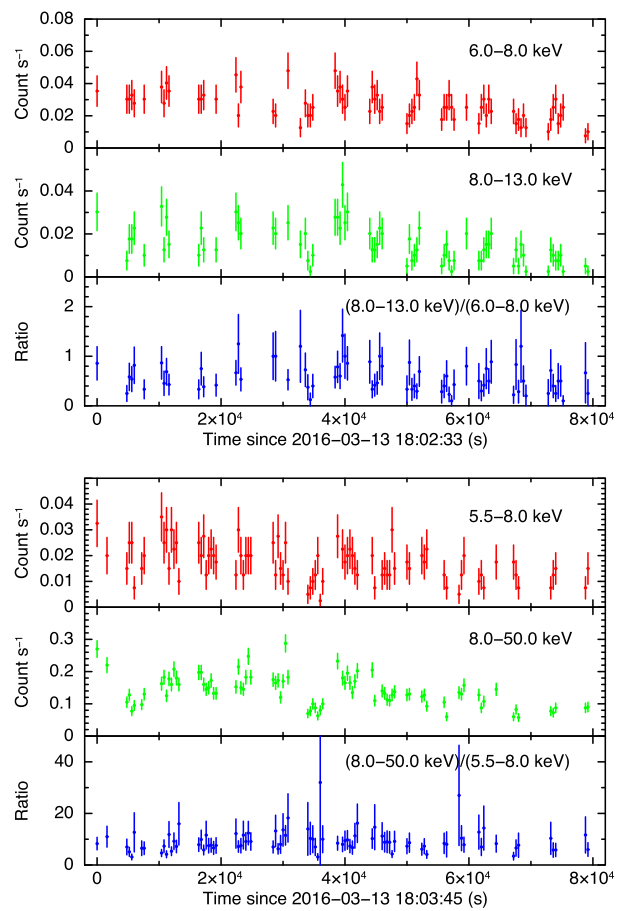


Fig. 6. Light curves of the SXI (top) and HXI-1 (bottom) with 400 s resolution. The energy bands dominated by the fluorescence lines (red) and continuum emission (green) are shown with the ratio between the two bands (blue). (Color online)

(SXI), while that of the fluorescence line band is < 0.25 (HXI-1) and < 0.15 (SXI).

A pulsation search was performed for both SXI and HXI-1 light curves in each band shown in figure 6, and also in the entire band. After the search from 1 s to one tenth of the exposure time of each instrument, we found no significant periodic pulsation. This prevents any conclusive determination that the compact object is a neutron star.

Because there was no apparent outburst during the exposure, we extracted the spectra of the SXI and HXI-1 without any distinction of time. NXB for SXI was calculated using `sxinxngen`, which considers both the magnetic COR weighting of the observation and the position of the source extracting region in the CCD. To maximize the statistics, we subtracted only the NXB component rather than extracting background spectrum from the surrounding region for the SXI. We extracted all events during the good time interval of each instrument, and hence the extracted durations are not precisely coincident between the SXI

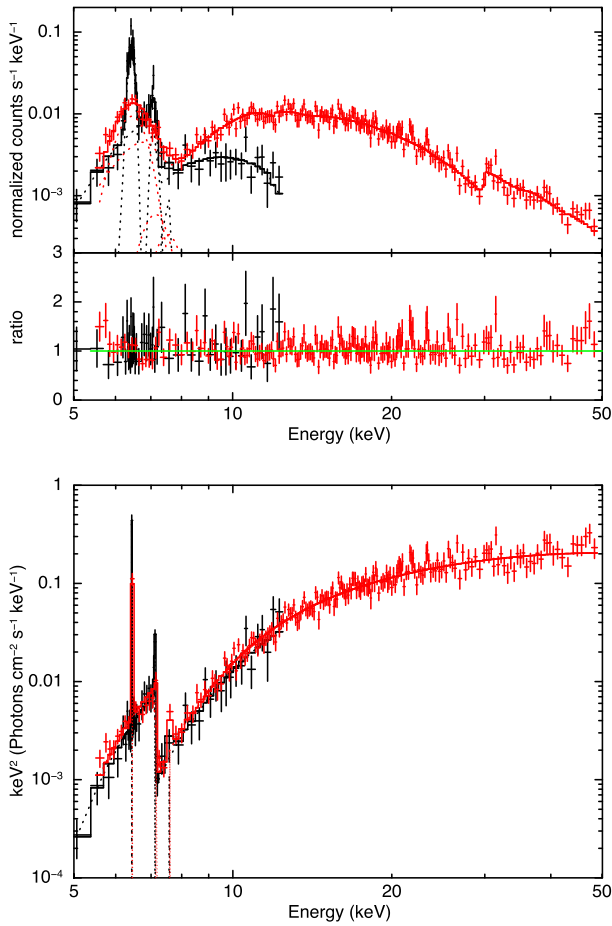


Fig. 7. Top: Spectra obtained with the SXI (black) and HXI-1 (red). The best-fit spectral model is drawn with solid lines. Each model component is designated with dashed lines. Bottom: Unfolded spectra using the best-fit model A summarized in table 2. Color coding is the same as that in the top panel. (Color online)

and HXI-1. In top panel figure 7, we applied a model of $\text{tbvarabs}*\{\text{cutoffpl}+\text{gau}+\text{gau}+\text{gau}\}$ (hereafter model A). We set the Fe abundance of the absorbing material to be free to reproduce both of the low-energy extinction and the Fe absorption edge, while the abundances of other elements were fixed to solar values. The difference between model A and the model adopted in Barragán et al. (2009) is that we represent the fluorescence lines from the excitation states with different total angular momenta ($K\alpha_1$ and $K\alpha_2$, $K\beta_1$ and $K\beta_3$) with a single Gaussian function, while Barragán et al. (2009) introduced a Gaussian function for each fluorescence line. Considering that the Fe $K\alpha$ line width measured with the SXS is negligible for the SXI and HXI-1, the widths of the Gaussian functions are fixed to be zero. Furthermore, the line centroid of Ni $K\alpha$ is fixed so that the ratio of the centroids of Fe $K\alpha$ and Ni $K\alpha$ becomes the value in Hölzer et al. (1997). We also introduced a constant factor that is multiplied by the HXI-1 data to account for possible inter-instrument calibration uncertainty of the

Table 2. Best-fit parameters for the SXI and HXI-1 spectra.

Parameter	Model A	Model B
N_{H} (10^{24} cm^{-2})	$2.06^{+0.21}_{-0.09}$	$2.19^{+0.10}_{-0.06}$
A_{Fe}	$1.19^{+0.09}_{-0.14}$	0 (fixed)
E_{edge}	N/A	$7.108^{+0.025}_{-0.046}$
τ_{MAX}	N/A	$2.32^{+0.15}_{-0.26}$
Γ	$0.74^{+0.29}_{-0.24}$	$0.50^{+0.02}_{-0.06}$
E_{C}^* (keV)	$37.8^{+19.3}_{-19.0}$	$30.9^{+10.0}_{-1.9}$
A ($10^{-3} \text{ cm}^{-2} \text{ s}^{-1}$)	$4.7^{+0.3}_{-3.2}$	$2.4^{+0.1}_{-0.2}$
E (Fe $K\alpha$) (keV)	$6.426^{+0.011}_{-0.010}$	$6.427^{+0.011}_{-0.011}$
EW (Fe $K\alpha$) (keV)	2.15	2.09
I (Fe $K\alpha$) ($10^{-3} \text{ cm}^{-2} \text{ s}^{-1}$)	$2.2^{+0.8}_{-0.5}$	$1.6^{+0.2}_{-0.2}$
E (Fe $K\beta$) (keV)	$7.101^{+0.051}_{-0.001}$	$7.108^{+0.014}_{-0.028}$
EW (Fe $K\beta$) (keV)	0.38	0.49
I (Fe $K\beta$) ($10^{-4} \text{ cm}^{-2} \text{ s}^{-1}$)	$1.9^{+0.9}_{-0.7}$	$1.8^{+1.2}_{-0.7}$
I (Ni $K\alpha$) ($10^{-4} \text{ cm}^{-2} \text{ s}^{-1}$)	<4.0	$2.1^{+1.8}_{-1.7}$
Constant factor	1.177	1.213
χ^2 (d.o.f.)	245.0 (251)	250.3 (249)

*Exponential cutoff energy in the power-law model.

effective area. An edge-like structure seen slightly below 30 keV is due to an edge in the quantum efficiency of the CdTe double-sided strip detectors, and hence is not seen in the unfolded spectrum shown in the bottom panel of figure 7.

The best-fit parameters are summarized in table 2. A comparison of the spectral parameters with those obtained from the Suzaku observation in 2006 (Barragán et al. 2009) shows that the flux of the continuum and line components significantly decreased in a ten-year interval while the equivalent widths increased. The unabsorbed luminosities in the 2–10 keV band are 1.0×10^{34} and $5.0 \times 10^{35} \text{ erg s}^{-1}$, assuming the distances to the target to be 0.9 and 6.2 kpc, respectively. This is much less than the Eddington limit of $1.8 \times 10^{38} \text{ erg s}^{-1}$ for a neutron star of $1.4 M_{\odot}$, and is consistent with values derived for the vast majority of HMXBs, even if including correction for the partial blockage of the continuum source, as discussed in section 4.

The Fe K-shell absorption edge energy is another key parameter that strongly depends on the ionization state of the reprocessing materials. In order to explore this we add an edge model that gives

$$f'(E) = \begin{cases} f(E) & (E < E_{\text{edge}}), \\ f(E) \cdot \exp[-\tau_{\text{MAX}}(E/E_{\text{edge}})^{-3}] & (E \geq E_{\text{edge}}), \end{cases} \quad (1)$$

where E_{edge} and τ_{MAX} are the edge position and the absorption depth at the edge, respectively. Because the edge model accounts for absorption at the edge position, we set the

Fe abundance of the tbvarabs to zero in our spectral fitting. The results are given in table 2 in the column labeled model B.

Evaluating the flux of the possible Compton shoulder was performed by adding another Gaussian function to model A with its centroid and width (1σ) which are fixed to 6.3 keV and 50 eV, respectively (Matt 2002). There is no significant flux of the additional line with its 90% upper limit of $5.4 \times 10^{-4} \text{ cm}^{-2} \text{ s}^{-1}$, which corresponds to the 90% upper limit of the equivalent width of 103 eV.

4 Discussion

The Fe line in IGR J16318 contains information about the ionization state and kinematics of the emitting gas via the profile shape. It also contains information about the quantity and geometrical distribution of the emitting gas via the line strength, i.e., the flux or equivalent width. This does not necessarily yield unique determinations of interesting physical quantities, but can strongly constrain them under various scenarios. General discussions of the dependence of flux or equivalent width have been provided by many authors (e.g., Koyama 1985; Makishima 1986; Torrejón et al. 2010; Giménez-García et al. 2015).

In particular, in the simplest case of a point source of continuum producing the Fe K line via fluorescence at the center of a spherical uniform cloud, simple analytic calculations show that the line equivalent width is approximately proportional to the equivalent hydrogen column density (N_{H}) of the cloud for $N_{\text{H}} \leq 1.5 \times 10^{24} \text{ cm}^{-2}$. At a greater N_{H} the gas becomes Thomson thick and the equivalent width no longer increases. The maximum equivalent width is 1–2 keV and depends on the Fe elemental abundance and on the shape of the SED of the continuum source in the energy band above ~ 6 keV. For the solar Fe abundance and an SED consisting of a power-law with a photon index of 2, the maximum attainable equivalent width is less than 2 keV. Numerical calculations for toroidal reprocessors show that the Thomson thin approximation breaks down at N_{H} , much less than $1.5 \times 10^{24} \text{ cm}^{-2}$ (Yaqoob et al. 2010).

Equivalent widths greater than 2 keV can be obtained if the reprocessor is not spherically symmetric around the continuum source, i.e., if there is an opaque screen along the direct line of sight to the continuum source. This is the most likely explanation for large equivalent widths observed from X-ray binaries during an eclipse (e.g., Watanabe et al. 2006), or Seyfert 2 galaxies (Krolik & Kallman 1987; Koss et al. 2016). This provides a likely explanation for the large equivalent width observed from IGR J16318; it is crudely consistent with the column density we measured, $N_{\text{H}} \simeq 2.1 \times 10^{24} \text{ cm}^{-2}$, together with at least a partial blockage of

the continuum source by a structure that has a Thomson depth much greater than unity. We thus predict that the true luminosity of the source is greater than what we infer from simple dilution at a distance of 0.9–6.2 kpc, by a factor of 2.

We derived the line centroid of Fe K α in spite of low photon statistics. The weighted average of the energies at the maxima of the seven Lorentzian functions is $6399.1^{+2.5}_{-2.6}$ eV if we consider the gain shift and the uncertainty of the SXS. Our result is consistent with those obtained with CCD detectors aboard XMM-Newton (Ibarra et al. 2007) and Suzaku (Barragán et al. 2009). However, the uncertainty of the measurement was significantly dispelled by the SXS. We must consider the systematic velocity and the orbital velocity of the reprocessor. According to the NIR spectroscopy, there is no significant systemic velocity of the companion star with $c\Delta\lambda/\lambda = -110 \pm 130 \text{ km s}^{-1}$ (Filliatre & Chaty 2004). If we assume the masses of the companion star and the compact object to be $30 M_{\odot}$ and $1.4 M_{\odot}$, respectively, the line-of-sight velocity of the compact object with respect to the companion star is within $\pm 155 \text{ km s}^{-1}$. Then, the total Doppler velocity is expected to be $-110 \pm 200 \text{ km s}^{-1}$, corresponding to a shift of 2.3 ± 4.3 eV.

The top panel of figure 8 shows a theoretical value of the Fe K α line centroid (E_{line}) versus the ionization state (Palmeri et al. 2003; Mendoza et al. 2004; Yamaguchi et al. 2014). Comparing those with the measured values, the ionization state of Fe I–X is preferred. This is in agreement with other HMXBs reported by Torrejón et al. (2010). On the other hand, the line centroid measured with the SXI and HXI-1 formally conflicts, at the 90% confidence level, with that measured with the SXS. Monitoring the pulse heights of the onboard calibration ^{55}Fe source by the SXI (Nakajima et al. 2018) reveals that the pulse heights disperse in the range of ~ 2 –3 ch, which corresponds to ~ 12 –18 eV. This can be interpreted as a systematic uncertainty on the SXI energy scale, which brings the SXI + HXI-1 into marginal agreement with the SXS.

The middle panel of figure 8 shows the absorption edge of the Fe (E_{edge}) as a function of the ionization state (Kallman et al. 2004; Bearden & Burr 1967). The edge energy measured with the SXI and HXI-1 strongly constrains the ionization state to be no higher than Fe III, which is consistent with that obtained with the Fe K α line centroid. Even if we consider the gain uncertainty of the SXI, as noted above, the ionization state is no higher than Fe IV. We also plot the difference between E_{edge} and E_{line} in the bottom panel because such a difference is rather robust against the inaccurate energy scale. Although the result suggests the very cold reprocessor, Fe I–IV is possible if we introduce a Doppler shift of $\sim 1000 \text{ km s}^{-1}$ (see later for a justification

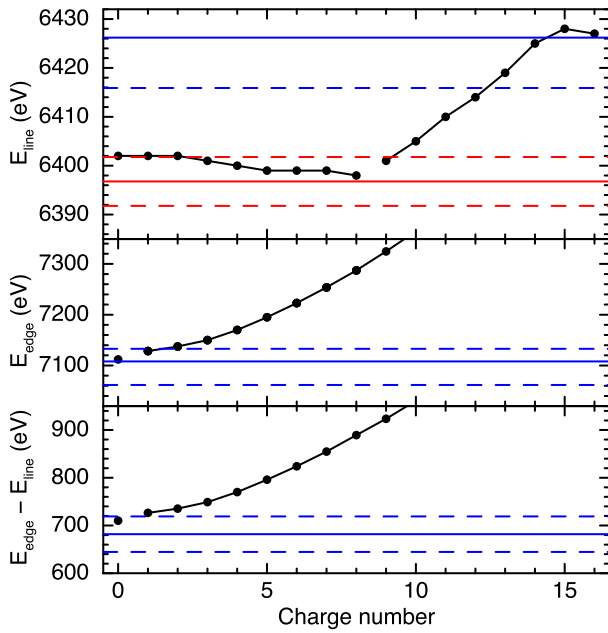


Fig. 8. Top: Fe K α line centroid (E_{line}) as a function of the ionization state calculated by Yamaguchi et al. (2014) from the expectation by Palmeri et al. (2003) (charge number ≤ 8) and Mendoza et al. (2004) (charge number ≥ 9). Values measured with the SXS and SXI+HXI-1 are shown by the red and blue solid lines, respectively. The gain shift of +1 eV and the most probable systematic velocity of the reprocessor are corrected for the SXS. The dashed lines designate the 90% confidence level. Middle: Fe K-shell ionization energy (E_{edge}) as a function of the ionization state expected by Kallman et al. (2004) (charge number ≥ 1) and Bearden and Burr (1967) (charge number = 0). Values measured with the combined spectra of the SXI and HXI-1 is shown by the blue solid line and the statistical error range is by the dashed line. Bottom: Difference between E_{edge} and E_{line} is plotted together with the measured value with the SXI and HXI-1. (Color online)

of this assumed value). Barragán et al. (2009) also discuss the ionization state of Fe with the statistically best spectrum. Although their line centroid value, itself, does not reject the slightly ionized state, they claim that the reprocessing materials are neutral, considering the systematic uncertainty of the gain of Suzaku/XIS (Koyama et al. 2007). Here, we develop the discussion with the updated and upgraded data obtained with Hitomi.

Kallman et al. (2004) calculated the abundance distribution of the Fe ions in a photoionized plasma as a function of the ionization parameter, $\xi = L/nR^2$ (Tarter et al. 1969), where n is the gas density, R is the distance between the X-ray source of ionizing radiation and the gas, and L is the luminosity of the continuum emission. The range of the ionization states Fe I–IV is consistent with an ionization parameter value of $\log(\xi) \lesssim -2$. The distance between the X-ray source and the gas responsible for the Fe emission, R , can be estimated based on the X-ray time variability. Walter et al. (2003) estimated the distance to be $R \simeq 10^{13}$ cm with XMM-Newton by the maximum delay observed between

the Fe K α line and the continuum variations. Light curves derived from other observations (Ibarra et al. 2007) also exhibited that Fe K α line followed almost immediately the continuum. Applying $R \simeq 10^{13}$ cm, we estimated the gas density (n) and the thickness of the reprocessing materials along the line of sight (l) to be $n \gtrsim 3 \times 10^{10} \text{ cm}^{-3}$ and $l = N_{\text{H}}/n \lesssim 7 \times 10^{13}$ cm, respectively. If we consider the ~ 80 d orbit and the masses of the companion star and the compact object as above, the distance between them is 2×10^{13} cm. The maximum size of the reprocessor l and R may be comparable with the system size.

One of the most likely candidates for the reprocessor is cold stellar wind from the massive companion star. The wind velocity (v_w) at a distance of r can be estimated assuming the typical β -law,

$$v_w = v_\infty (1 - R_*/r)^\beta, \quad (2)$$

where v_∞ is the terminal velocity and R_* is the stellar radius. Assuming the commonly used $\beta = 0.5$ and $r = 2 R_*$, we obtain $v_w/v_\infty \sim 0.7$. When we assign a typical v_∞ of the early type stars of $\sim 1500\text{--}2000 \text{ km s}^{-1}$ (Abbott 1978), $v_w \sim 1050\text{--}1400 \text{ km s}^{-1}$ is obtained. The measured Fe K α line width is equivalent to $v = 160_{-70}^{+300} \text{ km s}^{-1}$. This is much less than the Doppler broadening expected from speeds that are characteristic of similar systems. This indicates that the line-emitting region does not cover the whole region of the stellar wind, including the companion star. It suggests that the line may be produced in a relatively small region centered on the compact object. In this case, the line centroid will be Doppler-shifted, depending on the orbital phase of the compact object. When we shift both the line centroid and the K-shell edge energy by 25 eV, which corresponds to v_w of 1250 km s^{-1} , the two estimates of the ionization state contradict each other. This implies that the preferred orbital phase is ~ 0.25 or ~ 0.75 . However, v_∞ distributes over a wide range, even among members of the supergiant HMXBs (Giménez-García et al. 2016). Furthermore, Manousakis and Walter (2011) argue that highly absorbed HMXB systems have lower wind velocities than do classical supergiant HMXBs. An atmosphere model for the donor of Vela X-1 by Sander et al. (2018) also expects that the wind velocity at the neutron star location is significantly lower than that predicted by the β -law. A more accurate determination of v_∞ of the companion star is needed for further discussion. Another interesting possibility is discussed by Torrejón et al. (2015) for supergiant HMXBs. These authors argue that Fe K α must be produced close to the photosphere of the donor star, where the wind is still in the acceleration zone—in the region facing the compact object. This case agrees with the fact that the reprocessor does not cover the X-ray source completely. The SXS established an empirical upper limit

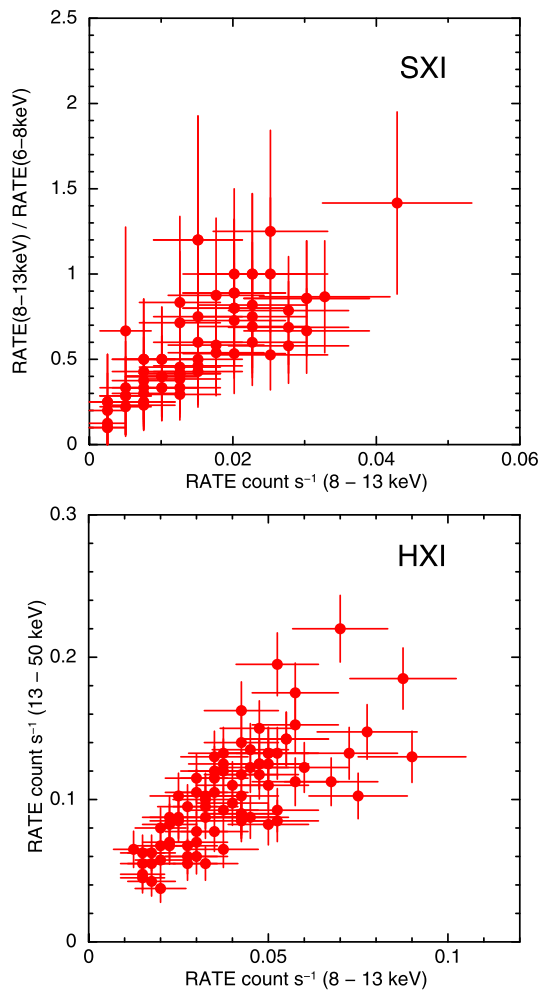


Fig. 9. Top: Intensity ratio of the continuum band to the fluorescence-line band versus the intensity in the former band for the SXI. The bin size is 400 s. Bottom: Count light curves of 13–50 keV band obtained with the HXI-1 versus those in the 8–13 keV band. (Color online)

to the Fe $K\alpha$ width that would imply stellar wind velocities at distances of $1.06 R_*$ – $1.10 R_*$. This is in agreement with theoretical predictions on the onset of wind clumps given by Sundqvist and Owocki (2013).

To investigate the time variability of the line and continuum emissions obtained in this observation, we plot the ratio of the continuum flux to the fluorescence-line flux as a function of the former for the SXI in the top panel of figure 9. The clear positive correlation indicates that the continuum component exhibits variability with a larger dynamical range than the line component, as measured with the fractional variation of the light curves in subsection 3.2. In other words, at least part of the line emission does not follow the continuum variability on time scales of less than 400 s. This is consistent with the results obtained by Ibarra et al. (2007) with XMM-Newton. One possible explanation for the positive correlation is that the continuum is produced in a compact region while the line emission takes

place in a significantly extended region. Another possibility is the time variation of the column density on the line of sight. Because the X-ray flux around the Fe K band can be affected by the absorption column, time variation of the absorption column on the line of sight can cause time variation only in the low energy band. To clarify this, we check the correlation between the count light curves in the 8–13 keV and 13–50 keV bands with the HXI-1 as shown in the bottom panel of figure 9. The clear positive correlation is a hint of the intrinsic variation of the continuum rather than being due to the changes in the intervening column density.

The absence of the Compton shoulder is confirmed, since it was in the spectrum obtained by Suzaku (Barragán et al. 2009), making a clear contrast with another strongly absorbed HMXB GX 301–2 (Watanabe et al. 2003; Fürst et al. 2011). Walter et al. (2003) and Ibarra et al. (2007) point out that the absence of a Compton shoulder can be due to an inhomogeneous distribution of reprocessing material. Another possibility is smearing of the Compton shoulder due to the free electrons with a temperature of several eV (Watanabe et al. 2003) and/or to the scattering with neutral hydrogen (Sunyaev & Churazov 1996; Sunyaev et al. 1999). In fact, mid-infrared observations of IGR J16318 by Chaty and Rahoui (2012) revealed a spectral component with a temperature of ~ 37000 – 40000 K. Since this temperature is higher than those of typical B1 supergiant stars, they suggest that the component corresponds to dense and hot material surrounding the stellar photosphere and is irradiated by X-rays from the compact object. Deeper exposure with high spectral resolution like the SXS is required for a further understanding of the circumstellar environment of this system.

5 Summary

In spite of such observing challenges as the large offset angle, and issues, such as cross-talk for the SXI, we analyzed photons from the target for all of the instruments that had been started up at the time of the Hitomi observation of IGR J16318. The microcalorimeter spectrum resolved the Fe $K\alpha_1$ and $K\alpha_2$ lines for the first time in an X-ray binary system and revealed that the line width is narrower than that compatible with the full range of speeds expected from a stellar wind. Combining the line centroid measured by the SXS and the energy of the Fe K-shell absorption edge by SXI+HXI-1, we put a constraint on the ionization state of the reprocessing materials to be in the range of Fe I–IV. Judging from the ionization parameter, the density and thickness of the materials are estimated. As reported in the past observations, the absorption is extraordinarily strong ($N_H > 10^{24} \text{ cm}^{-2}$) and the Compton shoulder component

is not apparent. These characteristics can be attributed to reprocessing materials that are distributed in a narrow solid angle or scattering primarily by warm free electrons or neutral hydrogen.

The Hitomi observation of IGR J16318 measured the width and energy of the Fe K fluorescence line with the precision that is unprecedented for an X-ray binary. The line reveals a line width and line shift that are much less than the Doppler broadening and Doppler shift expected from speed characteristic of similar systems. This was achieved using the SXS detection of 19 photons. If the aspect stability and accuracy of the Hitomi pointing system had been accurate at a few arcmin level, we would have obtained far more detailed diagnostics for the Fe K line and its absorption edge. However, this was not achieved in the initial operations of the Hitomi mission. We now know that the physics of the Fe K line is considerably different for this object, and perhaps for other X-ray binaries, from the physics previously assumed despite 40 years of detailed study and more. Thus, microcalorimeter observations of X-ray binaries in the future with the X-ray recovery mission will open up a new and exciting field of study.

Author contributions

H. Nakajima led this research in data analysis and writing manuscript. He also contributed to the SXI hardware design, fabrication, integration and tests, in-orbit operation, and calibration. K. Hayashida provided key comments on the whole discussion. He also made hardware and software contributions to the SXI as one of the instrument principal investigators. T. Kallman contributed for discussion primarily on the Fe line diagnostics and to elaborate the manuscript. T. Miyazawa worked for the fabrication and calibration of the Hard X-ray Telescope. H. Takahashi contributed to the timing analyses of the HXI. He also made software and hardware contributions to the HXI. M. Guainazzi led observation planning and gave critical comments mainly on the reprocessing materials. H. Awaki, T. Dotani, C. Ferrigno, L. C. Gallo, P. Gandhi, C. A. Kilbourne, P. Laurent, K. Mori, K. Pottschmidt, C. S. Reynolds, and M. Tsujimoto improved the manuscript.

Acknowledgments

We thank the support from the JSPS Core-to-Core Program. We acknowledge all the JAXA members who have contributed to the ASTRO-H (Hitomi) project. All U.S. members gratefully acknowledge support through the NASA Science Mission Directorate. Stanford and SLAC members acknowledge support via DoE contract to SLAC National Accelerator Laboratory

DE-AC3-76SF00515. Part of this work was performed under the auspices of the U.S. DoE by LLNL under Contract DE-AC52-07NA27344. Support from the European Space Agency is gratefully acknowledged. French members acknowledge support from CNES, the Centre National d'Études Spatiales. SRON is supported by NWO, the Netherlands Organization for Scientific Research. Swiss team acknowledges support of the Swiss Secretariat for Education, Research and Innovation (SERI). The Canadian Space Agency is acknowledged for the support of Canadian members. We acknowledge support from JSPS/MEXT KAKENHI grant numbers JP15H00773, JP15H00785, JP15H02070, JP15H02090, JP15H03639, JP15H03641, JP15H03642, JP15H05438, JP15H06896, JP15K05107, JP15K17610, JP15K17657, JP16H00949, JP16H03983, JP16H06342, JP16J02333, JP16K05295, JP16K05300, JP16K05309, JP16K13787, JP16K17667, JP16K17672, JP16K17673, JP17H02864, JP17K05393, JP21659292, JP23340055, JP23340071, JP23540280, JP24105007, JP24540232, JP24684010, JP25105516, JP25109004, JP25247028, JP25287042, JP25400236, JP25800119, JP26109506, JP26220703, JP26400228, JP26610047, JP26670560, and JP26800102. The following NASA grants are acknowledged: NNX15AC76G, NNX15AE16G, NNX15AK71G, NNX15AU54G, NNX15AW94G, and NNG15PP48P to Eureka Scientific. This work was partly supported by Leading Initiative for Excellent Young Researchers, MEXT, Japan, and also by the Research Fellowship of JSPS for Young Scientists. H. Akamatsu acknowledges support of NWO via Veni grant. C. Done acknowledges STFC funding under grant ST/L00075X/1. A. Fabian and C. Pinto acknowledge ERC Advanced Grant 340442. P. Gandhi acknowledges JAXA International Top Young Fellowship and UK Science and Technology Funding Council (STFC) grant ST/J003697/2. Y. Ichinohe and K. Nobukawa are supported by the Research Fellow of JSPS for Young Scientists. N. Kawai is supported by the Grant-in-Aid for Scientific Research on Innovative Areas “New Developments in Astrophysics Through Multi-Messenger Observations of Gravitational Wave Sources”. S. Kitamoto is partially supported by the MEXT Supported Program for the Strategic Research Foundation at Private Universities, 2014–2018. B. McNamara and S. Safi-Harb acknowledge support from NSERC. T. Dotani, T. Takahashi, T. Tamagawa, M. Tsujimoto and Y. Uchiyama acknowledge support from the Grant-in-Aid for Scientific Research on Innovative Areas “Nuclear Matter in Neutron Stars Investigated by Experiments and Astronomical Observations”. N. Werner is supported by the Lendület LP2016-11 grant from the Hungarian Academy of Sciences. D. Wilkins is supported by NASA through Einstein Fellowship grant number PF6-170160, awarded by the Chandra X-ray Center, operated by the Smithsonian Astrophysical Observatory for NASA under contract NAS8-03060.

We thank contributions by many companies, including in particular, NEC, Mitsubishi Heavy Industries, Sumitomo Heavy Industries, and Japan Aviation Electronics Industry. Finally, we acknowledge strong support from the following engineers. JAXA/ISAS: Chris Baluta, Nobutaka Bando, Atsushi Harayama, Kazuyuki Hirose, Kosei Ishimura, Naoko Iwata, Taro Kawano, Shigeo Kawasaki, Kenji Minesugi, Chikara Natsukari, Hiroyuki Ogawa, Mina Ogawa, Masayuki Ohta, Tsuyoshi Okazaki, Shin-ichiro Sakai, Yasuko Shibano, Maki Shida, Takanobu Shimada, Atsushi Wada, Takahiro Yamada; JAXA/TKSC: Atsushi Okamoto, Yoichi Sato, Keisuke Shinozaki, Hiroyuki Sugita; Chubu Univ.: Yoshiharu Namba; Ehime Univ.: Keiji Ogi; Kochi Univ. of Technology: Tatsuro Kosaka; Miyazaki Univ.: Yusuke Nishioka; Nagoya Univ.: Housei Nagano;

NASA/GSFC: Thomas Bialas, Kevin Boyce, Edgar Canavan, Michael DiPirro, Mark Kimball, Candace Masters, Daniel McGuinness, Joseph Miko, Theodore Muench, James Pontius, Peter Shirron, Cynthia Simmons, Gary Sneiderman, Tomomi Watanabe; ADNET Systems: Michael Witthoef, Kristin Rutkowski, Robert S. Hill, Joseph Eggen; Wyle Information Systems: Andrew Sargent, Michael Dutka; Noqi Aerospace Ltd: John Doty; Stanford Univ./KIPAC: Makoto Asai, Kirk Gilmore; ESA (Netherlands): Chris Jewell; SRON: Daniel Haas, Martin Frericks, Philippe Laubert, Paul Lowes; Univ. of Geneva: Philipp Azzarello; CSA: Alex Koujelev, Franco Moroso.

References

- Abbott, D. C. 1978, *ApJ*, 225, 893
- Agarwal, B. K. 1979, *X-ray spectroscopy: an introduction* (Berlin: Springer-Verlag)
- Angelini, L., et al. 2018, *J. Astron. Telesc. Instrum. Syst.*, 4, 011207
- Arnaud, K. A. 1996, in *ASP Conf. Ser.*, 101, *Astronomical Data Analysis Software and Systems V*, ed. G. H. Jacoby & J. Barnes (San Francisco: ASP), 17
- Awaki, H., et al. 2016, in *Proc. SPIE*, 9905, *Space Telescopes and Instrumentation 2016: Ultraviolet to Gamma Ray*, ed. J.-W. A. den Herder et al. (Bellingham, WA: SPIE), 990512
- Barragan, L., Wilms, J., Kreykenbohm, I., Hanke, M., Fuerst, F., Pottschmidt, K., & Rothschild, R. E. 2010, in *Proc. 8th INTEGRAL Workshop "The Restless Gamma-ray Universe"*, PoS(INTEGRAL 2010), 135
- Barragán, L., Wilms, J., Pottschmidt, K., Nowak, M. A., Kreykenbohm, I., Walter, R., & Tomsick, J. A. 2009, *A&A*, 508, 1275
- Bearden, J. A., & Burr, A. F. 1967, *Rev. Mod. Phys.*, 39, 125
- Bodaghee, A., Tomsick, J. A., Rodriguez, J., & James, J. B. 2012, *ApJ*, 744, 108
- Cash, W. 1979, *ApJ*, 228, 939
- Chaty, S., & Rahoui, F. 2012, *ApJ*, 751, 150
- Coleiro, A., & Chaty, S. 2013, *ApJ*, 764, 185
- Courvoisier, T. J.-L., Walter, R., Rodriguez, J., Bouchet, L., & Lutovinov, A. A. 2003, *IAU Circ.*, 8063
- de Vries, C. P., et al. 2018, *J. Astron. Telesc. Instrum. Syst.*, 4, 011204
- Filliatre, P., & Chaty, S. 2004, *ApJ*, 616, 469
- Fujimoto, R., et al. 2016, in *Proc. SPIE*, 9905, *Space Telescopes and Instrumentation 2016: Ultraviolet to Gamma Ray*, ed. J.-W. A. den Herder et al. (Bellingham, WA: SPIE), 990535
- Fürst, F., et al. 2011, *A&A*, 535, A9
- Gehrels, N. 1986, *ApJ*, 303, 336
- Giménez-García, A., et al. 2016, *A&A*, 591, A26
- Giménez-García, A., Torrejón, J. M., Eikmann, W., Martínez-Núñez, S., Oskinova, L. M., Rodes-Roca, J. J., & Bernabéu, G. 2015, *A&A*, 576, A108
- Hölzer, G., Fritsch, M., Deutsch, M., Härtwig, J., & Förster, E. 1997, *Phys. Rev. A*, 56, 4554
- Ibarra, A., Matt, G., Guainazzi, M., Kuulkers, E., Jiménez-Bailón, E., Rodriguez, J., Nicastro, F., & Walter, R. 2007, *A&A*, 465, 501
- Iyer, N., & Paul, B. 2017, *MNRAS*, 471, 355
- Jain, C., Paul, B., & Dutta, A. 2009, *Res. Astron. Astrophys.*, 9, 1303
- Kallman, T. R., Palmeri, P., Bautista, M. A., Mendoza, C., & Krolik, J. H. 2004, *ApJS*, 155, 675
- Kelley, R., et al. 2018, *J. Astron. Telesc. Instrum. Syst.*, submitted
- Kilbourne, C. A., et al. 2018, *PASJ*, 70, 18
- Koss, M. J., et al. 2016, *ApJ*, 825, 85
- Koyama, K. 1985, in *Proc. Japan-US Seminar on Galactic and Extragalactic Compact X-Ray Sources*, ed. Y. Tabaka & W. H. G. Lewin (Tokyo: Institute of Space and Astronautical Science), 153
- Koyama, K., et al. 2007, *PASJ*, 59, S23
- Krivonos, R. A., Tsygankov, S. S., Mereminskiy, I. A., Lutovinov, A. A., Sazonov, S. Y., & Sunyaev, R. A. 2017, *MNRAS*, 470, 512
- Krolik, J. H., & Kallman, T. R. 1987, *ApJ*, 320, L5
- Lebrun, F., et al. 2003, *A&A*, 411, L141
- Lin, D., Webb, N. A., & Barret, D. 2012, *ApJ*, 756, 27
- Liu, Q. Z., van Paradijs, J., & van den Heuvel, E. P. J. 2006, *A&A*, 455, 1165
- Lutovinov, A., Revnivtsev, M., Gilfanov, M., Shtykovskiy, P., Molokov, S., & Sunyaev, R. 2005, *A&A*, 444, 821
- Lutovinov, A. A., Revnivtsev, M. G., Tsygankov, S. S., & Krivonos, R. A. 2013, *MNRAS*, 431, 327
- Maeda, Y., et al. 2018, *PASJ*, in press
- Makishima, K. 1986, in *The Physics of Accretion onto Compact Objects*, ed. K. O. Mason et al. (Berlin: Springer-Verlag), 249
- Manousakis, A., & Walter, R. 2011, *A&A*, 526, A62
- Matt, G. 2002, *MNRAS*, 337, 147
- Matt, G., & Guainazzi, M. 2003, *MNRAS*, 341, L13
- Mendoza, C., Kallman, T. R., Bautista, M. A., & Palmeri, P. 2004, *A&A*, 414, 377
- Miroshnichenko, A. S. 2007, *ApJ*, 667, 497
- Mitsuda, K., et al. 2007, *PASJ*, 59, S1
- Murakami, H., Dotani, T., & Wijnands, R. 2003, *IAU Circ.*, 8070
- Nakajima, H. 2017, *Nucl. Instrum. Meth. Phys. Res. A*, 873, 16
- Nakajima, H., et al. 2018, *PASJ*, 70, 21
- Nakazawa, K., et al. 2018, *J. Astron. Telesc. Instrum. Syst.*, submitted
- Noda, H., et al. 2016, in *Proc. SPIE*, 9905, *Space Telescopes and Instrumentation 2016: Ultraviolet to Gamma Ray*, ed. J.-W. A. den Herder et al. (Bellingham, WA: SPIE), 99053R
- Palmeri, P., Mendoza, C., Kallman, T. R., Bautista, M. A., & Meléndez, M. 2003, *A&A*, 410, 359
- Rahoui, F., Chaty, S., Lagage, P.-O., & Pantin, E. 2008, *A&A*, 484, 801
- Revnivtsev, M. G. 2003, *Astron. Lett.*, 29, 644
- Sander, A. A. C., Fürst, F., Kretschmar, P., Oskinova, L. M., Todt, H., Hainich, R., Shenar, T., & Hamann, W.-R. 2018, *A&A*, 610, A60
- Sundqvist, J. O., & Owocki, S. P. 2013, *MNRAS*, 428, 1837
- Sunyaev, R. A., & Churazov, E. M. 1996, *Astron. Lett.*, 22, 648
- Sunyaev, R. A., Uskov, D. B., & Churazov, E. M. 1999, *Astron. Lett.*, 25, 199
- Takahashi, T., et al. 2018, *J. Astron. Telesc. Instrum. Syst.*, submitted
- Tanaka, T., et al. 2018, *J. Astron. Telesc. Instrum. Syst.*, 4, 011211
- Tarter, C. B., Tucker, W. H., & Salpeter, E. E. 1969, *ApJ*, 156, 943
- Torrejón, J. M., Schulz, N. S., Nowak, M. A., & Kallman, T. R. 2010, *ApJ*, 715, 947
- Torrejón, J. M., Schulz, N. S., Nowak, M. A., Oskinova, L., Rodes-Roca, J. J., Shenar, T., & Wilms, J. 2015, *ApJ*, 810, 102

- Tsujimoto, M., et al. 2018, *J. Astron. Telesc. Instrum. Syst.*, 4, 011205
- Ubertini, P., et al. 2003, *A&A*, 411, L131
- Walter, R., et al. 2003, *A&A*, 411, L427
- Walter, R., et al. 2004, in *The INTEGRAL Universe*, ed. V. Schoenfelder et al. (ESA SP-552) (Noordwijk: ESA), 417
- Watanabe, S., et al. 2003, *ApJ*, 597, L37
- Watanabe, S., et al. 2006, *ApJ*, 651, 421
- Wilms, J., Allen, A., & McCray, R. 2000, *ApJ*, 542, 914
- Winkler, C., et al. 2003, *A&A*, 411, L1
- Yamaguchi, H., et al. 2014, *ApJ*, 780, 136
- Yaqoob, T., Murphy, K. D., Miller, L., & Turner, T. J. 2010, *MNRAS*, 401, 411